The Potential of Casing Treatments for Transonic Compressors: Evaluation Based on Axial-Slot and Rotor Blade Optimization

Georgios Goinis, Christian Voß and Eberhard Nicke
georgios.goinis@dlr.de
German Aerospace Center (DLR)
Institute of Propulsion Technology
Linder Hoehe, 51147 Koeln, Germany

ABSTRACT

Casing treatments (CTs) have proven their potential to increase the working range of a compressor stage, sometimes even with little or no decrease in efficiency. However, a positive impact on efficiency is only possible if the additional CT-losses are compensated by a reduction of other losses, especially at rotor tip. This appears to be increasingly difficult to achieve for highly efficient modern rotors. In order to analyse how CTs can contribute to improve the overall compressor design, extensive optimization studies are performed, aiming at increasing the stability and efficiency of a transonic compressor stage. Axial-slot CTs and the rotor are optimized separately with a high number of geometric parameters. Selected Pareto-optimal geometries of the two optimizations are combined to study various CTs on different rotors. It is shown that a significant increase in stability can be achieved using axial-slot CTs, exceeding the values that can be reached optimizing the rotor without CTs. However, no combination of optimized rotors and CTs is found that dominates the other geometries in terms of efficiency. Hence, the question whether a CT can contribute to an improved compressor design very much depends on the desired stage design. CTs provide a benefit if a maximum stability range is necessary or if certain design choices lead to a demand for a stability enhancement, that otherwise cannot be achieved. In order to gain a maximum efficiency, a design without CTs appears to be more promising in the first place. Designs with comparably high losses in the rotor tip region, e.g. due to large tip clearances, might also benefit of CTs in terms of efficiency.

Keywords: Casing Treatment; Transonic Compressor; Design; Optimization

NOMENCLATURE

Abbreviations

ADP	Aerodynamic Design Point
AxCT	Axial Slot Casing Treatment
CT	Casing Treatment
DLR	German Aerospace Center
MVDR	Meridional Velocity Density Ratio
NS	Near Stall
OP	Operating Point
S	Stall
SM(C)	Stability/Surge Margin (Criterion)

Symbols

c	Constraint
c	Chord
$\dot{m}$	Mass flow rate
o	Objective
ζ	Tip leakage flow angle, between chord and leakage flow
η	Isentropic efficiency
Π_{tot}	Total pressure ratio

1.0 INTRODUCTION

The design of a compressor stage for a desired total pressure ratio and mass flow aims at a maximum efficiency whilst providing the required stability margin. This can be expressed in terms of an optimization problem with two objectives, increased efficiency and stability. As these are conflicting design objectives, the result of such an optimization is a sum of Pareto-optimal solutions forming a Pareto-front. The question arises how CTs will influence such a Pareto-front and if the Pareto-optimum or parts of it consist of designs with CTs.

CTs can increase the working range of a compressor stage, in some cases even with little or no influence on efficiency [1]. However, these results are often obtained with rotors of low efficiency, as compared to the state of the art [2]. In general, the performance of a CT does not only depend on the CT itself but also on the rotor it is applied to. A positive effect on efficiency through a CT can only be achieved if the additional CT losses are overcompensated by a reduction of other losses. For sophisticated rotor designs this appears to be increasingly unlikely.

Some design trends can be for the benefit of designs with CTs, as they require an increased stability. Among these are a continuous increase in stage loading as well as a trend towards smaller core engines and thus higher relative tip clearances. This may also go along with a lower number of blades that can be fitted and the requirement of additional measures to achieve the necessary stability. In some studies the blade count has already deliberately been reduced in order to regain the loss in stability through the application of CTs, in expectation of higher overall efficiencies [3–7].

So far hardly any conclusions can be drawn, whether CTs can actually lead to future compressor designs with higher efficiencies that can not be achieved without CTs. In general, studies with only one rotor and a few CT designs are not capable of answering this question and a more extensive methodology is needed, to gain some insight. The

obvious approach, a simultaneous optimization of CTs, rotor blades and possibly also the stator, still lies beyond what is achievable with the current computational resources.

In this work, the potential of axial-slot CTs for improved designs is evaluated based on separate optimizations of a reference rotor and the CT. Some of the optimization results have already been presented in previous studies [8,9]. The study at hand provides a further analysis and comparison of these results. In this regard, the optimizations can be seen as a tool to provide Pareto-fronts which are the basis for further evaluation. Different Pareto-optimal CTs and rotor designs are combined in order to estimate a mutual Pareto-front and analyze how CTs can improve compressor design.

A similar study but using circumferential grooves has been shown in [9,10]. Due to the limited stability margin increase achievable using circumferential grooves in comparison to axial-slots, no advantage could be identified over a rotor blade optimization. As axial-slot CTs achieve higher stability enhancements, they are chosen for the study at hand.

2.0 REFERENCE COMPRESSOR

2.1 Rig250 - General Overview

The study is based on Rig250 (figure 1), a DLR research compressor. Specifically, the transonic stage 1 lies in the focus of this work. Rig250 consists of four stages and an IGV, representing a scaled-down version of the front stages of a modern highly loaded stationary gas turbine compressor. Some key characteristics of Rig250 (stage1) are listed in table 1.

Rotational speed	N	12960 1/min
Mass flow rate, reduced	$\dot{m}_{red}$	46.3 kg/s
Total pressure ratio	Π_{tot}	4.83
Ma at rotor 1 tip inlet	Ma_{rel}	1.21

Table 1: Rig250 design parameters.

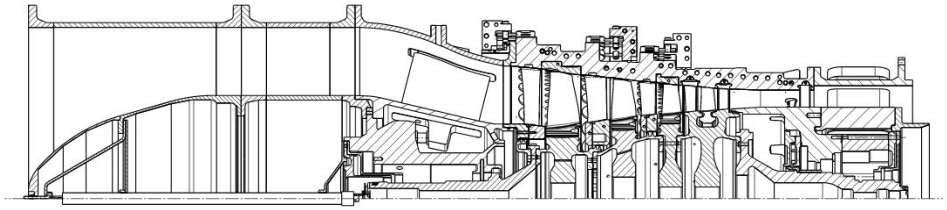

Figure 1: Rig 250.

2.2 Aerodynamics at the stability limit at reduced speed

In this work, an extension of the stability margin at 90% speed is studied. At this speed, stage 1 is the first to reach its stability limit with spike type stall occuring in rotor 1.

To optimize the rotor stability, it has to be made sure that always the rotor fails when throttling the stage and not the stator, even assuming a significant improvement in rotor stability through the optimization. This is ensured by closing the variable stator 1 by 8° according to the VGV schedule, reducing the risk of flow separation in stator 1 and increasing the loading of rotor 1. Doing so will remove a possible influence of the stator design on the results. However, it should be noted that an optimization of the rotor or the application of a CT will always impact the flow of the stator and has to be considered for the final compressor design.

Close to the stability limit, the flow at the rotor tip is dominated by a strong interaction of the tip leakage vortex with the shock resulting in a vortex-burst and a pronounced

area of blockage. Figure 2 shows the vortex core trajectories for different operating points along a speed line. Operating points beyond the stability limit do not converge to a stable solution, but diverge. Yet, they complete the picture of the flow at stall.

As the throttling is increased, the shock moves upstream and the length of the vortex core flow before hitting the shock decreases (figure 3). At the same time, the shock increases in intensity, whereas the axial momentum of the vortex core flow reduces. This can be attributed to the fact that the angle of the tip leakage flow near the rotor leading edge increases when throttling the rotor (figure 4) and, due to the reduced length, the vortex can travel until it hits the shock, which leaves less time to reenergize the flow through mixing processes. The result is a stronger shock-vortex-interaction and increased areas of blockage in the tip region when approaching the stability limit.

Simulating the same stage using time-accurate CFD, a vortex, periodically shedding from the leading edge, can be observed, as has also been reported in the literature for transonic rotors prone to spike type stall [11–15].

Based on this analysis, CTs can be regarded as a promising measure to influence the stability limiting flow features and extend the stall margin of the rotor.

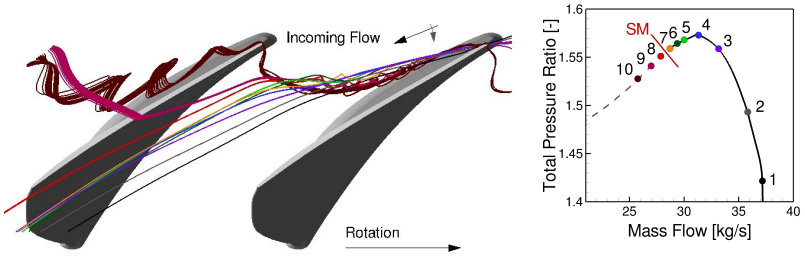

Figure 2: Tip leakage vortex core trajectory at different operating points. OP8-OP10 are beyond the numerical stability limit and do not represent stable numerical solutions.

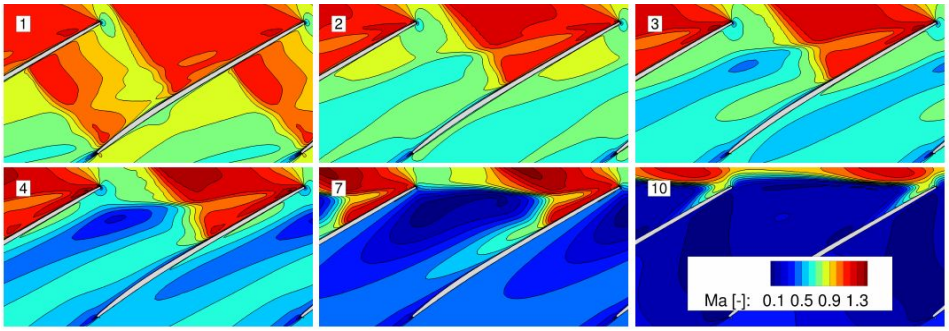

Figure 3: Ma contours at a S1-plane close to tip for different operating points.

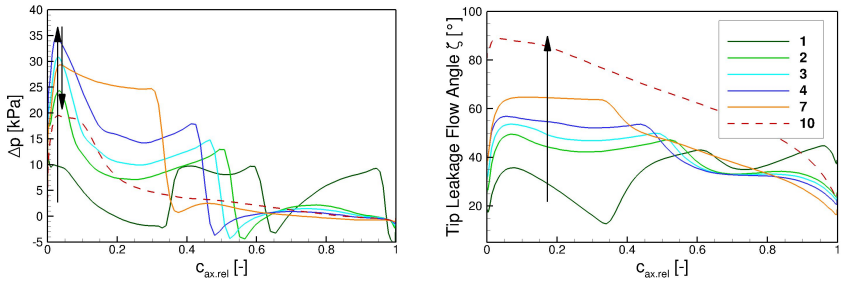

Figure 4: Tip leakage flow at different operating points.

3.0 OPTIMIZATION SETUP

3.1 General considerations and optimization strategy

Automated optimizations of CTs have high demands in terms of computational resources. This can be attributed to two circumstances. First, in order to optimize CTs, the stability margin needs to be determined for every new geometry during the optimization. A highly accurate determination of the numerical stability margin requires significant computational effort [16]. Second, most types of CTs require the use of time accurate CFD. This increases the demand for computational resources significantly as compared to steady-state methods.

Hence, the number of possible geometry evaluations during the optimization that can be achieved within a reasonable amount of time and resources is limited. Yet, a certain number of individuals (geometries that are evaluated) is needed for an optimization to achieve a satisfactory state of convergence. This number depends, among other things, on the complexity of the optimization problem and therefore mainly on the parametrization and the total number of parameters of the geometry to be optimized.

Recent developments, specifically the possibility to perform multi-objective optimizations with the use of Co-Kriging surrogate models, reduces the computational resources needed for the optimization by speeding up its convergence. Yet, they do not eliminate the problem completely.

As a consequence, compromises are necessary in order to ensure a sufficient number of geometry evaluations and thus a convergence of the optimization towards a Pareto-front that will provide a solid basis for evaluation and analysis purposes.

The compromises can be made regarding the complexity of the optimization problem and the model accuracy used for each geometry evaluation. This involves many aspects of the optimization setup and some experience is needed to create an adequate setup. The goal can be described as a setup that uses as little computational power per geometry evaluation, but still correctly predicts the influence of geometry changes on the objectives on a qualitative scale.

3. 2 Parameterization

A parametric design that allows generating a wide range of different axial-slot CT geometries is used [8,17]. The parameterization of the CTs is based on a spline defined in a nondimensional x^* - r^* -plane and cross sections defined in a nondimensional x^* - y^* -plane as depicted in figure 5 and figure 6.

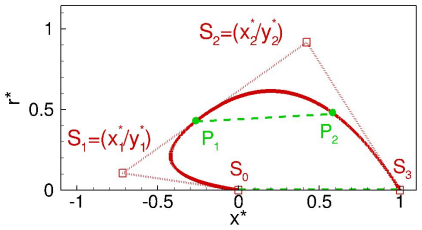

Figure 5: Spline in x^* - r^*

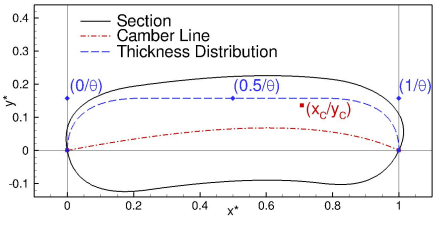

Figure 6: Section definition

The x^* - r^* -spline is defined by four knots: $S_0 = (0,0)$, $S_1 = (x_1^*, r_1^*)$, $S_2 = (x_2^*, r_2^*)$, $S_3 = (1,0)$. A section is defined via a camber line and a thickness distribution. The camber line is defined by a spline with three knots, $T_0 = (0,\theta)$, $T_1 = (0.5,\theta)$, $T_2 = (1,\theta)$, as is the thickness distribution, $C_0 = (0,0)$, $C_1 = (x_c, y_c)$, $C_2 = (1,0)$). Two sections that are similar in the nondimensional space are connected with the x^* - r^* -spline to form a 3D-skeleton. The first section is scaled and placed between

$S_0 = (0,0)$ and $S_3 = (1,0)$, the second between P_1 and P_2, where P_1 lies at 30% of the path length along the spine starting at S_0 and P_2 at 70% of the path length.

The transformation into the 3D-space includes a staggering by an angle γ and a shift of the upper section in circumferential direction θ_s to obtain a lean of the CT. The resulting 3D-skeleton is scaled and mapped on the casing. Its final size and position are defined by two points on the casing x_s and x_e, expressed as distances to the position of the rotor leading edge (figure 7 and figure 8).

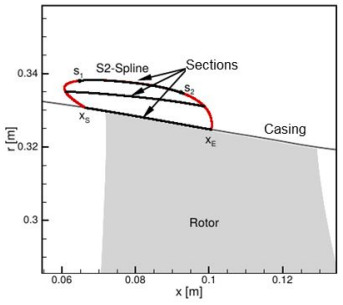

Figure 7: Placement of CT on top of rotor.

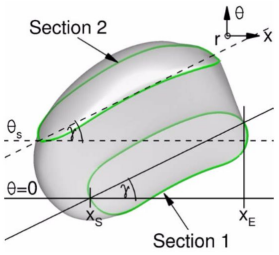

Figure 8: Final staggered and skewed CT.

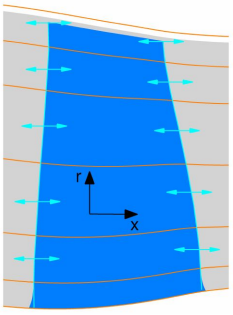

Figure 9: Rotor construction.

An automated process using a skinning algorithm is used to form the final CT geometry (figure 8). Four CTs are used per rotor. The number of CTs is fixed during the optimization. It is considered as the maximum number that can be fitted to the casing with the size of CTs aimed for. Previous studies have shown that the impact of higher numbers of CTs on stability margin and efficiency increases [17].

In total 11 CT-parameters are used. The values are chosen such that the CTs can be placed in the front part of the rotor, can have a high staggering and skew in both directions and provide a highly variable shape. Further details can be found in [8].

The rotor parameterization is based on seven airfoils defined on construction lines in the x-r-plane (orange lines in figure 9). The hub airfoil is kept unchanged. The rotor leading edge and trailing edge are defined via splines in the x-r-plane. The airfoils are scaled and stacked to fit between the leading and trailing edge. They are defined using a spline for the suction surface and a thickness distribution. In total 95 parameters are variables of the rotor optimization.

3.3 CFD Setup

The Navier-Stokes CFD-solver TRACE is used, which is being developed specifically for turbomachinery flows at the DLR Institute of Propulsion Technology [18,19]. Rotor and CT are simulated using a time accurate URANS method. IGV and stator are coupled to the rotor using a flux conserving mixing plane and simulated using RANS (figure 10). A k-ω turbulence model is used. The rotor optimization is entirely performed using RANS-CFD.

The core mesh used for the optimizations consists of approximately 1 million cells, with a radial resolution of 35 cells and a tip clearance resolution of 7 cells. The core mesh is structured whereas for the CT an unstructured mesh is used to enable an automated mesh generation for all different types of geometries, as described in [8]. CTs of the optimization have up to 100000 grid points. A wall function approach is used at all surfaces.

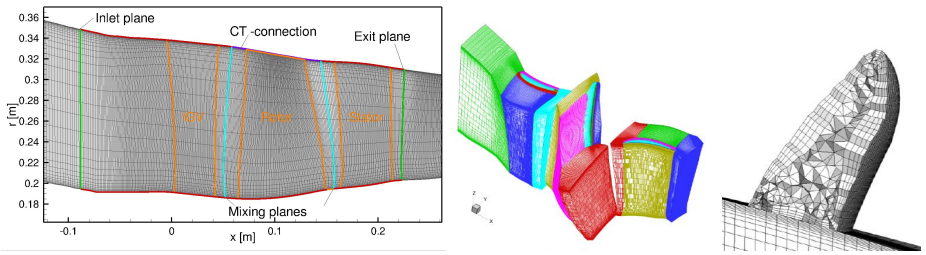

Figure 10: Meshing: S2 view or core (left), 3D view of core (middle), cut through CT (right).

3.4 Stability margin determination

An accurate determination of the numerical stability margin requires the simulation of several operating points in an iterative manner (figure 11, left). The numerical costs for such a procedure are high, limiting its use for optimization purposes. In this study, it is used for the rotor optimization using time-averaged RANS CFD. The CT optimization, however, could only be performed using time accurate URANS CFD. In combination with an iterative stability margin determination, this would exceed the computational resources available. Hence, for the CT optimization, a stability margin estimation based on a single operating point close to the stability limit is used.

The two approaches are depicted in figure 11. The iterative stability margin determination is basically a bisection algorithm. The back pressure is increased by units of Δp. For each increase in backpressure, an operating point is simulated, restarting on the previous converged solution. If the simulation does not lead to convergence, the pressure increment is halved, $\Delta p_{new} = \Delta p_{old}/2$, and the procedure repeated until $\Delta p < \varepsilon$, with $\varepsilon = 25Pa$. The last converged operating point is used for the calculation of the numerical stability limit.

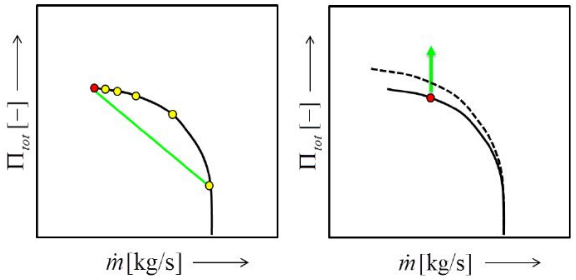

Figure 11: Comparison of different approaches to determine (left) or to estimate (right) the numerical stall margin.

A comparably cheap estimation of the stability margin is achieved by evaluating the properties of a single operating point close to the stability limit. The mass flow is fixed and the total pressure ratio is used as an estimate for the stability margin (figure 11, right). For the CT optimization, it is considered the best compromise between accuracy in stability margin estimation and the possible number of geometry evaluations during the optimization. This approach is capable of a general qualitative evaluation of different axial-slot CTs in terms of stability margin.

3.5 Optimization setup

The optimization tool used is *AutoOpti*, which is based on an evolutionary algorithm and makes extensive use of metamodels to accelerate the optimizations. *AutoOpti* can perform multi-objective, multi-fidelity optimizations using Co-Kriging metamodels [9,20–23]. It is being developed at the DLR Institute of Propulsion Technology.

Two objectives are defined. The first aims at increasing the efficiency close to working line conditions at 100% speed. For RANS optimizations the maximum efficiency is to be increased:

$$o_{1.RANS} := max(\eta_{is.max})! \mid n = 100\%N \qquad (1)$$

This is to avoid efficiency increases purely due to a radial redistribution of the flow, as has been observed in [10], and not due to a reduction of losses. A controller implemented into the CFD code allows approaching the point of maximum efficiency with high accuracy.

For the URANS CT-optimization, this procedure is too costly. Also, a positive effect on efficiency through a radial redistribution due to an axial-slot CT placed in the leading edge region has not been observed. Hence, the ADP is used in this case instead:

$$o_{1.URANS} := max(\eta_{is.ADP})! \mid n = 100\%N \qquad (2)$$

The second objective is to increase the stability margin. A stability margin criterion SMC defined between two operating points [24] is used. For the RANS rotor optimization it is based on the iterative stability margin determination:

$$o_{2.RANS} := max(SMC_I)! \;=\; \max\left(\frac{\Pi_{tot.S90}}{\Pi_{tot.WL90}} \cdot \frac{\dot{m}_{WL90}}{\dot{m}_{S90}} - 1\right)! \;\mid\; n = 90\%N \qquad (3)$$

The objective used for the URANS CT-optimization is based on the stability margin approximation, due to the otherwise too extensive computational costs:

$$o_{2.URANS} := max(SMC_A)! \;=\; \max\left(\frac{\Pi_{tot.NS90}}{\Pi_{tot.WL90}} \cdot \frac{\dot{m}_{WL90}}{\dot{m}_{NS90}} - 1\right)! \;\mid\; n = 90\%N \qquad (4)$$

The first operating point is a working line point OP_{WL90}, the second is the last converged operating point OP_{S90} for the RANS based rotor optimization or the near stall point OP_{NS90}, for the URANS CT optimization, respectively.

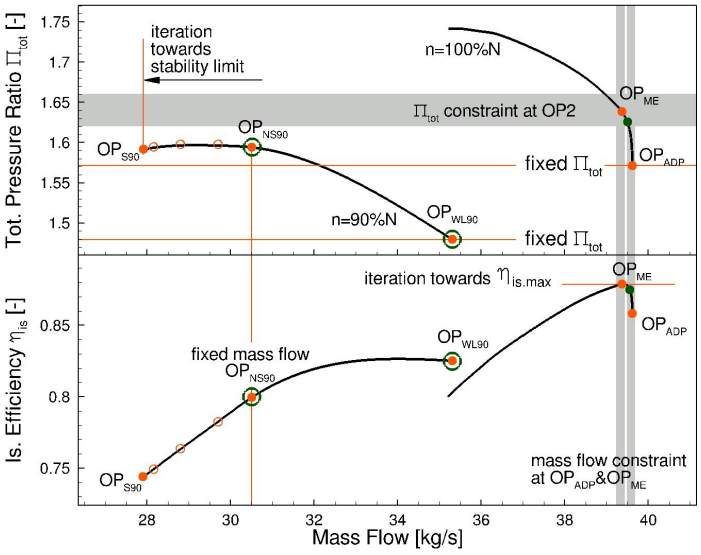

Figure 12: Operating points used for the optimizations.

For the rotor optimization, additional constraints are defined in order not to deviate significantly from the original design intent of the stage and guarantee comparability between the different optimization results. The aerodynamic constraints consist of a maximum allowed deviation of mass flow from the original design in OP_{ME} and OP_{ADP} of $\pm 0.3\%$ and of the total pressure ratio at OP_{ME} of $\pm 0.5\%$. OP_{ADP} is defined via a fixed total pressure ratio and adjusted using a PID-controller, as is OP_{WL90}. OP_{NS90} is fixed in mass flow. The blade stresses are checked to make sure the structural mechanics do not deteriorate. The operating points are depicted in figure 12.

In order to speed up the rotor optimization, a multi-fidelity approach is used as described in [9]. The low fidelity process chain consists of a limited number of operating points (marked green in figure 12) and a modified calculation of the fitness functions, but is capable of rough estimates, helping to speed up the optimization using Co-Kriging metamodels. In the following, however, only high-fidelity results will be discussed. Low-fidelity data was only used to improve the Co-Kriging models.

4.0 OPTIMIZATION STUDIES

Two optimizations, of the rotor and of axial-slot CTs, both performed to increase stability margin and efficiency, are performed. Most aspects of the optimizations are identical, to achieve good comparability. Yet, as not all aspects are identical, especially the stability margin evaluation and the use of time accurate and time-averaged CFD, a direct comparison is not possible and has been achieved by simulating selected results using URANS and an iterative stability margin determination.

4.1 Rotor Optimization

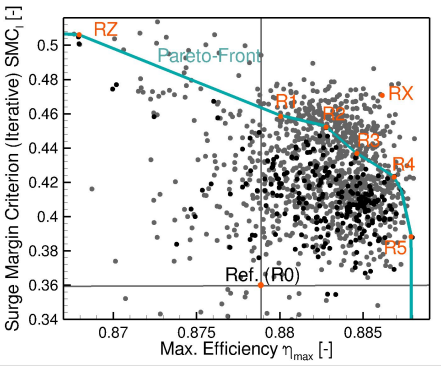

Figure 13: Rotor optimization database.

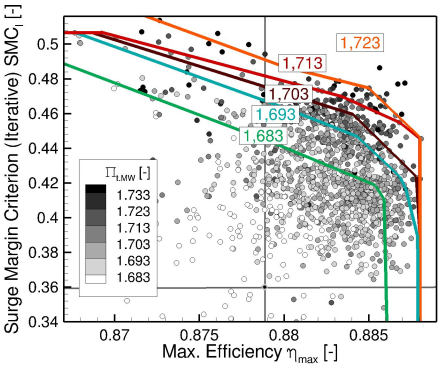

Figure 14: Change of Pareto-front depending on the total pressure ratio at max. efficiency.

Figure 13 shows the Pareto-front and the individuals of the optimization in terms of fitness function values. Black dots indicate geometries that fulfill all constraints. A significant increase of 27% in stability margin and 0.9%-points in efficiency can be achieved.

Figure 14 shows how the Pareto-front changes depending on the constraint for the maximum total pressure ratio in the point of maximum efficiency OP_{ME}. The constraint has a dominating influence on the resulting Pareto-front. If a higher pressure ratio is allowed, a further increase in stability margin and efficiency can be achieved.

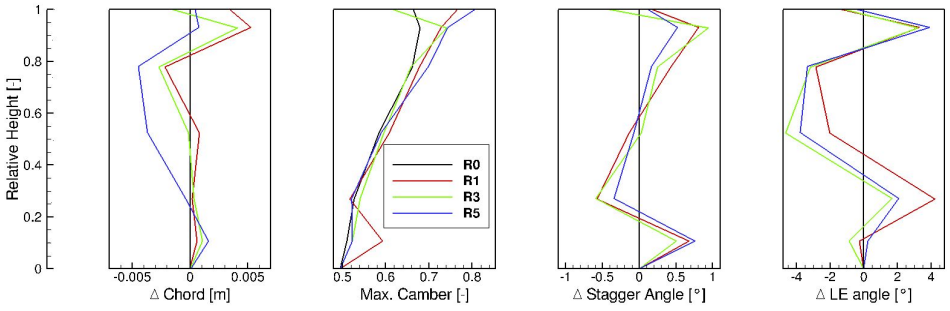

Figure 15: Radial distributions of rotor construction parameters.

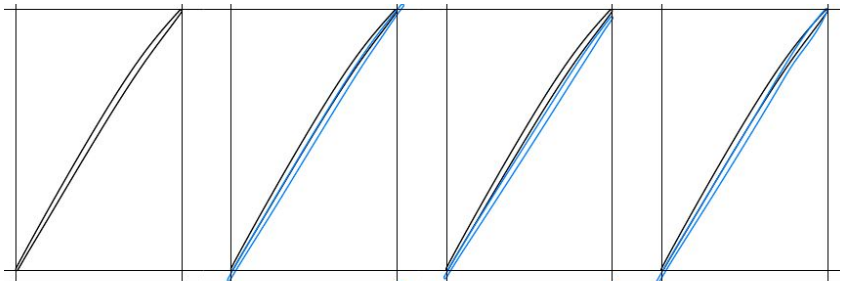

(a) R0 (b) R0 and R1 (c) R0 and R3 (d) R0 and R5

Figure 16: Tip airfoils of selected rotors.

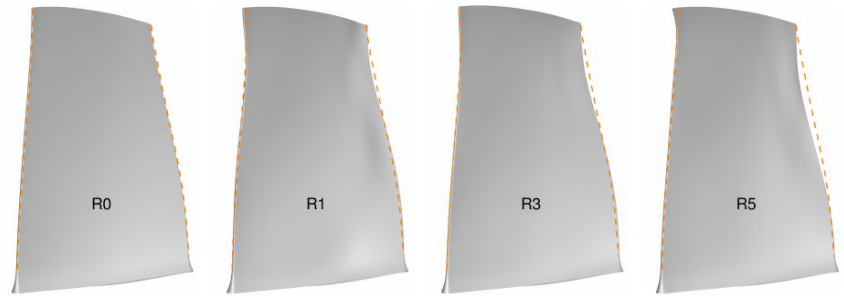

Figure 17: Selected rotor blades in x-r-plane. Leading and trailing edge of R0 highlighted.

All optimized rotors show a forward sweep and a slightly longer chord at the tip. At lower blade sections the chord is reduced. Stagger and leading edge angle at 90% span are increased and the leading edge angle between 40% and 80% span is reduced (figure 15). The tip aerofoils show less camber (figure 16) and even a slightly positive curvature for R1 in the front part and R5 in the rear part, that helps reducing shock losses via a slight pre-compression near stall (R1) or the working line (R5), respectively. Along the Pareto-Front the most significant change is in chord length between 30% and 90% span (R1->R5: chord decreases; figure 17).

A comparison of the two optimizations requires the RANS-based results to be simulated using URANS CFD. Selected Pareto-optimal rotors are simulated using URANS and the iterative stability margin determination. The result in terms of the objective functions is shown in figure 18. A shift in both maximum efficiency and stability margin criterion can be observed. However, the qualitative results remain the same.

Although it can not be expected that a URANS-based optimization yields exactly the same Pareto-front [25], based on the simulations shown in figure 18, it can be assumed that the deviation is small and the RANS Pareto-front is close to the URANS Pareto-front.

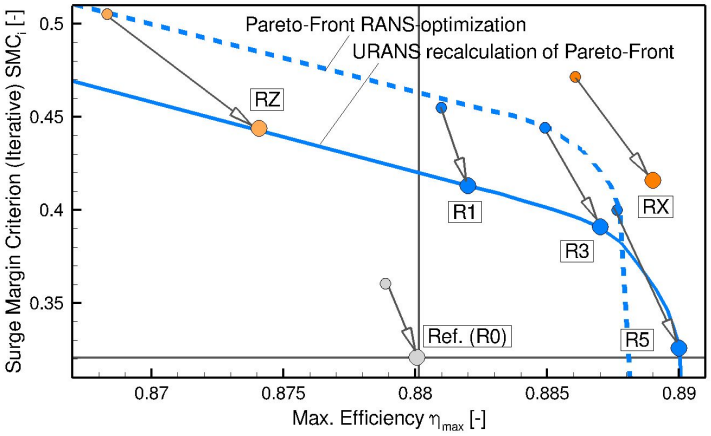

Figure 18: Recalculation of RANS results using URANS.

4.2 Axial-Slot-CT-optimization

In total around 300 different CT geometries have been simulated during the axial-slot CT optimization. Figure 19 shows the database. A significant increase of about 17% in stability margin SMC_A could be achieved. This translates into 46% SMC_I for AxCT1 using the iterative approach.

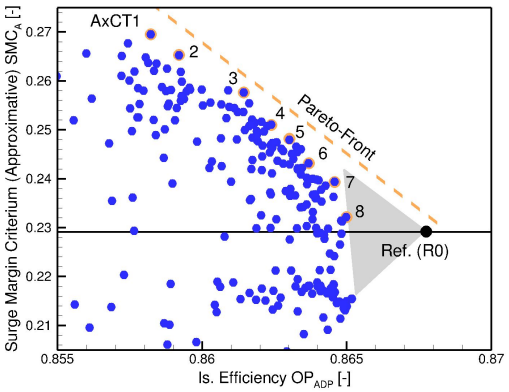

Figure 19: AxCT-optimization database.

The effect on efficiency, however, is negative for every CT geometry of the optimization. As the CT parameter boundaries were such that the CTs could not become very small in size there is a gap between the reference without CTs and the geometries with CTs.

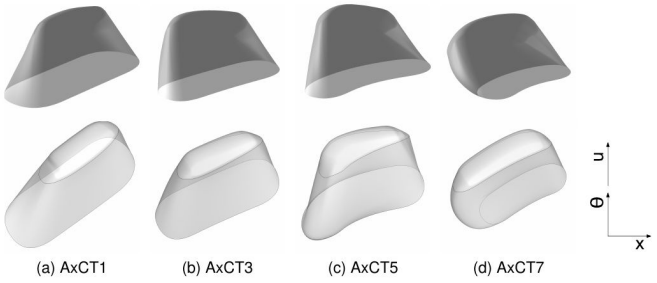

Figure 20: Pareto-optimal AxCTs.

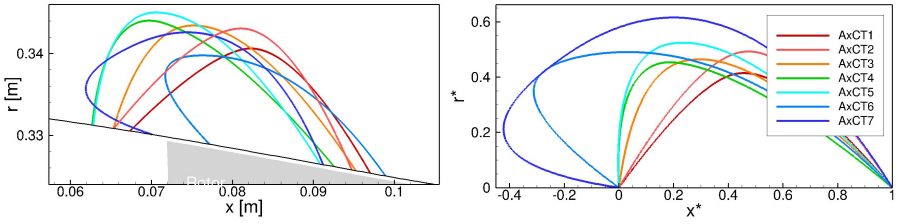

Figure 21: x-r-shape (left) and x*-r*-shape (right) of Pareto-optimal AxCTs.

All Pareto-optimal CTs are staggered opposite to the direction of the rotor staggering and leaned in direction of rotor rotation (figure 20). The position is above the rotor leading edge and a distinct change in $x-r-$shape can be observed along the Pareto-front (figure 21).

5.0 COMBINATIONS OF OPTIMIZED CTS AND ROTORS

Selected optimized rotors and CTs are combined in order to analyze the performance of axial-slot CTs on different rotors. Figure 22 shows speed lines of rotors R1, R3, R5, RX and RZ with and without AxCT1. Equally, combinations of AxCT3 and AxCT5 with

these rotors are analyzed. The results in terms of stability margin criterion and maximum efficiency are listed in table 2.

A significant improvement of the stability margin at 90% speed can be observed for all combinations. With CTs, higher total pressure ratios and lower mass flow rates are reached at 90% speed. The speedlines at 100% speed are steeper, reaching higher total pressure ratios as well. Regardless of the rotor combined with, AxCT1 shows the highest improvements of stability margin and AxCT5 the lowest. However, the effect on stability margin strongly depends on the rotor the CT is combined with.

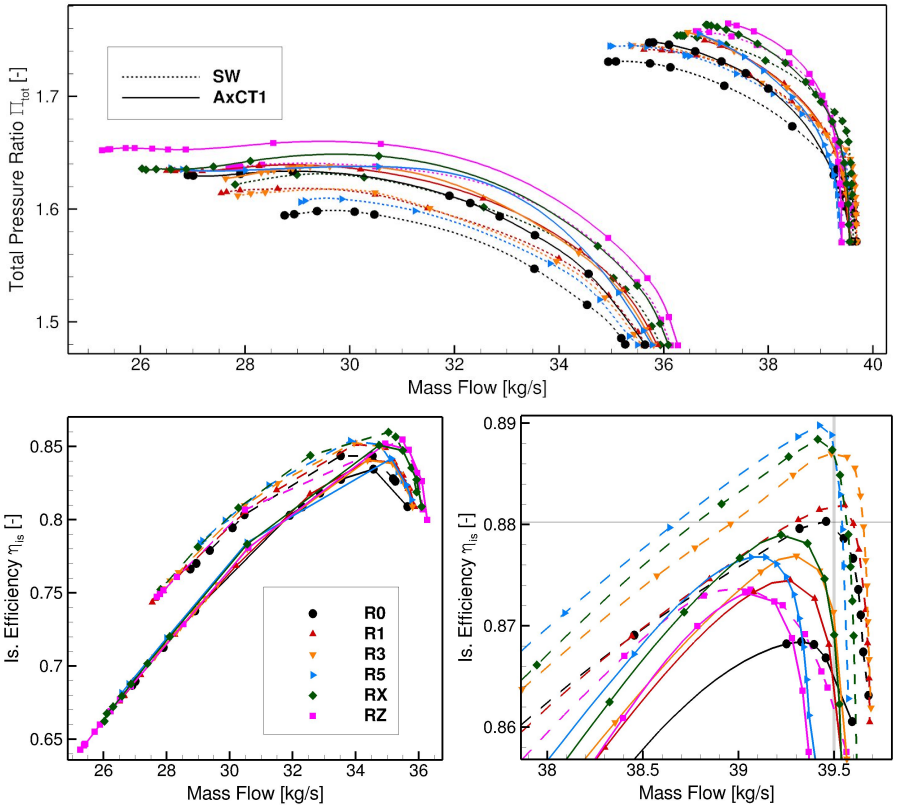

Figure 22: Speedlines of different rotors with and without AxCT1.

	SMC_I				$\Delta\eta_{max}$			
	SW	Ax5	Ax3	Ax1	SW	Ax5	Ax3	Ax1
R0	32,1	40,0	43,3	47,1	0	-0,4	-0,9	-1,2
R5	32,6	39,2	45,5	49,0	0	-0,5	-0,9	-1,3
R3	39,1	40,0	40,6	42,6	0	-0,5	-0,7	-1,0
R1	41,3	43,9	48,2	48,8	0	-0,3	-0,5	-0,8
RX	41,6	42,4	48,7	53,6	0	-0,4	-0,7	-0,9
RZ	44,4	44,4	51,9	58,1	0	0,2	0,0	0,0

Table 2: Performance of different rotor-CT-combinations.

A significant drop in efficiency can be observed applying CTs. This drop mainly depends on the CT and not on the rotor. R0-R5 and RX all show a similar reduction in efficiency depending on the CT. An exception is rotor RZ, which has been chosen to represent a configuration with comparably low efficiency. If combined with different axial-slots, no drop in efficiency is observed and even a slight increase in combination with AxCT5.

Additional aspects to consider are the aerodynamic constraints that have been applied during the rotor optimization. As the high total pressure ratios achieved with CTs exceed the constraints defined for the rotor optimization, an additional rotor RX is

examined. RX reaches equally high pressure ratios as R0-R5 combined with CTs. Therefore, RX also does not fulfill the constraint in total pressure ratio. It can be observed that RX does not achieve stability margins beyond those reached with CTs. Furthermore a decrease in choke mass flow rate at 100% speed can be observed when CTs are applied.

Figure 23 shows a plot of the objectives SMC_I vs. η_{max} of all results achieved using URANS simulations and a stability margin iteration. It shows different estimations of Pareto-fronts. The possible improvement without CTs is plotted as a blue line and with reduced aerodynamic constraint regarding the maximum total pressure at OP_{ME} as a dark blue line. The simulated rotors R0-R5, RX and RZ are highlighted, as well as combinations of these rotors with the AxCTs 1, 3, 5. The area in this plot that can be reached by combinations of rotors and CTs is indicated with an orange line. It can be observed that a specific area (orange) can only be reached with CTs. This is the case for high stability margins, especially if higher total pressure ratios are considered.

The analysis shows that CTs should be considered for stage designs when high stability margins have to be reached. Comparing rotors R1, R3 and R5, the best results with CTs are achieved using R5, which has been optimized for high efficiency. R1, which has been optimized for high stability margin, reaches equal values of stability margin in combination with CTs, but at lower efficiency. If a maximum efficiency is the aim, a design optimized for efficiency without CTs should be chosen.

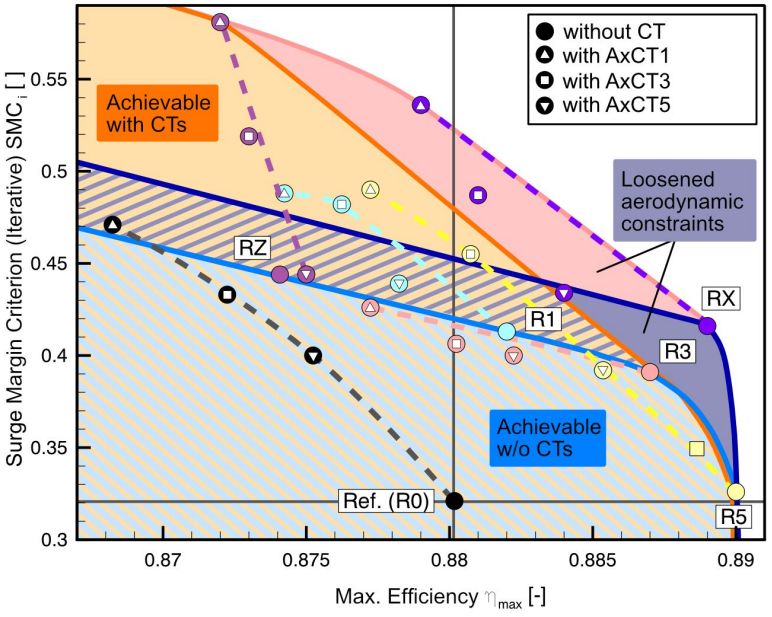

Figure 23: Performance of different rotor-CT-combinations.

6.0 AERODYNAMIC ANALYSIS

The working mechanism of the axial slots has been explained in literature in detail [8]. It is a combination of fluid extraction from the main flow in the downstream part of the CT, recirculation and injection of fluid into the main flow in the upstream part of the CT. The mechanism is driven by pressure differences across the shock and across the rotor blade. As the flow field at the interface to the CTs periodically changes with the rotor rotation, the recirculation through the CT is not continuous but interrupted.

Figure 24 shows how the pressure field at the interface of the CT changes over one period and how the flow recirculations develops and is interrupted again. The four timesteps shown in figure 24 can also be seen in figure 25 (a), which shows the radial component of the velocity at the rotor blade tip.

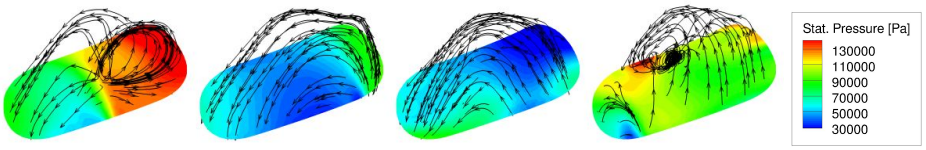

(a) t/T=0/4 (b) t/T=1/4 (c) t/T=2/4 (d) t/T=3/4

Figure 24: Snapshots at flow through AxCT1 at OP_{NS} .

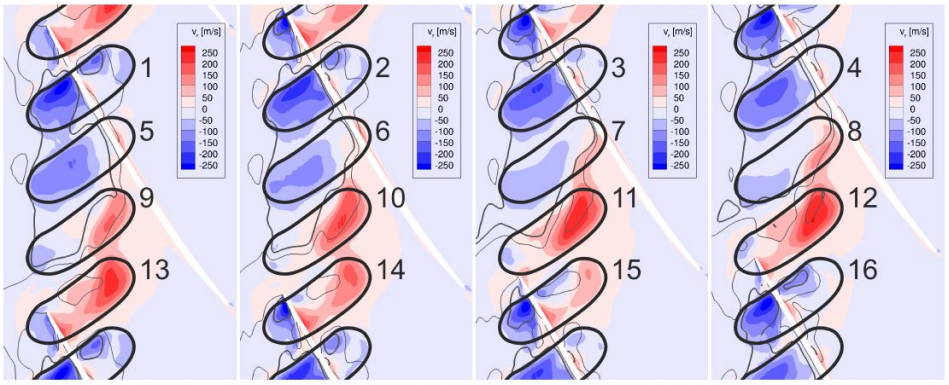

(a) t/T=0/16 (b) t/T=1/16 (c) t/T=2/16 (d) t/T=3/16

Figure 25: OP_{NS90} , S1 contour plot of radial velocity on a plane near the rotor tip.

Figure 25 shows four snapshots at different timesteps of all four CTs of a passage. Hence, the flow in and out of a CT at 16 different timesteps can be observed. It can be seen that fluid behind the shock is extracted from the main flow in the area where the blockage fluid spreads as a consequence of the shock-vortex-interaction. Flow is injected in the leading edge suction side area where the tip vortex develops.

Figure 26 shows the change in (time averaged) blockage area through the application of CTs. A significant reduction of blockage near the pressure side of the blade can be observed, allowing fluid to enter the passage and reducing the possibility of leading edge separations.

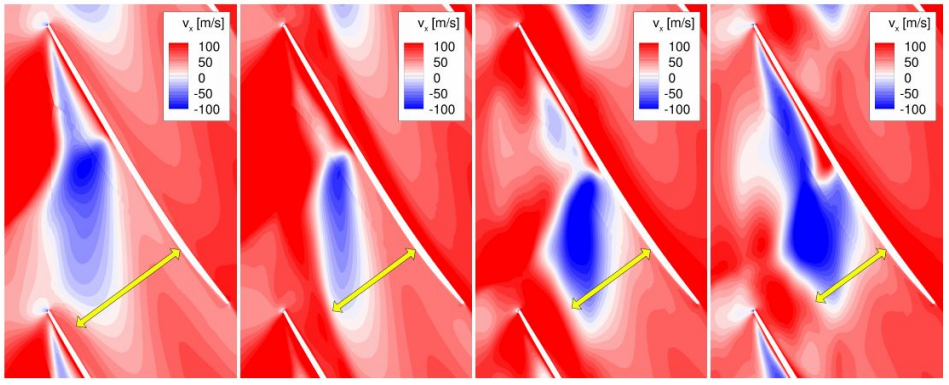

(a) Ref. w/o CT (b) AxCT7 (c) AxCT4 (d) AxCT1

Figure 26: OP_{NS90} , S1 contour plot of axial velocity on a plane near the rotor tip.

An interaction of the main flow with the CT happens at all operating points. Near the working line only a weak recirculation of flow through the CT can be observed, as the driving pressure difference is small. However, there is still a circulating flow inside the CTs and an interaction with the main flow increasing the losses in the rotor tip region. The result is a reduction of efficiency in the tip region at OP_{MW} , as can be seen in figure 27a.

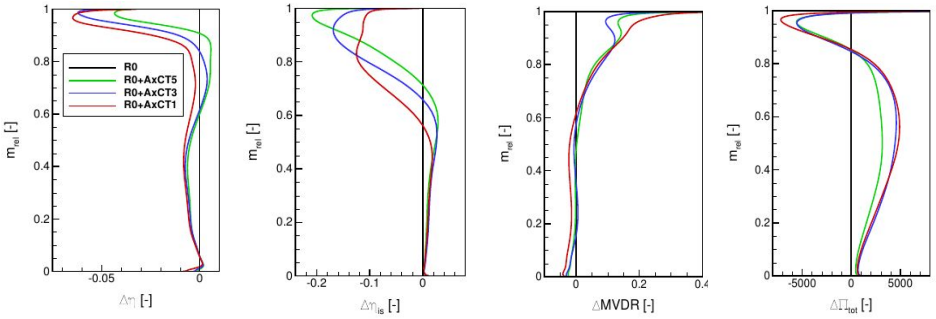

(a) OP_{MW} (b) OP_{NS90} (c) OP_{NS90} (d) OP_{NS90}

Figure 27: Stage 1 efficiency delta compared to R0 in OP_{MW} (a) and OP_{NS90} (b) . (c-d): OP_{NS90} , rotor MVDR delta and, total pressure ratio delta.

The reduction of blockage in the near stall operating point OP_{NS90} results in a radial redistribution of mass flow towards the casing (figure 27c). At the same time the efficiency near the casing reduces considerably (figure 27b). This can be attributed to a stronger interaction of the CT flow and the main flow as well as increasing shock losses due to increased pre-shock Mach-numbers. The total pressure increase across the rotor therefore reduces at tip and increases at lower blade sections (figure 27d). The tip section is less throttled at OP_{NS90} as compared to the reference R0.

A reduced throttling at tip can be also observed for the optimized rotors, however, it is less pronounced as figure 28 shows for OP_{MW} and OP_{NS90}. The shock is more downstream and of lower intensity.

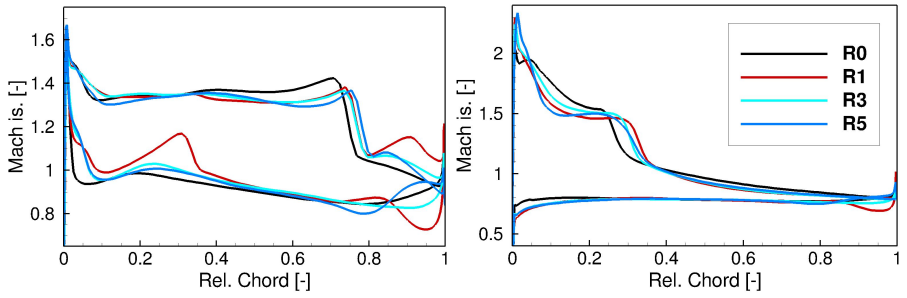

Figure 28: Is. Mach numbers of different rotors near tip at OP_{ME} (left) and OP_{NS90} (right).

The optimized rotors have an increased efficiency. The gain is pronounced in the area of the tip leakage vortex at approximately 90%-95% span (figure 29 a,b). The loss reduction increases near stall (figure 29 c). At the last stable operating point the losses of all rotors reach values in the tip region that lie closer together as compared to the near stall operating point (figure 29 d).

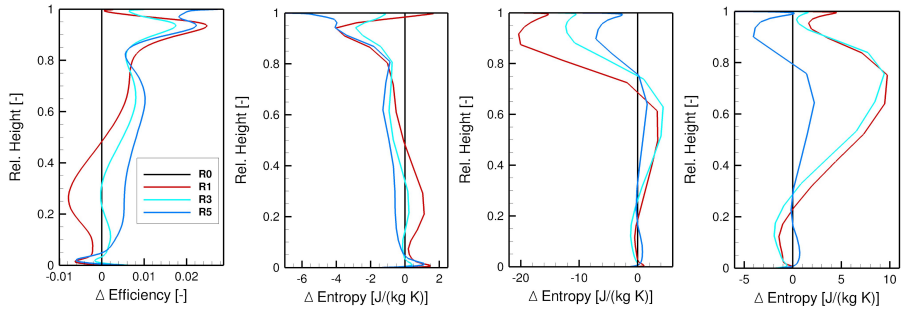

(a) OP_{ME} (b) OP_{ME} (c) OP_{NS90} (d) OP_{S90}

Figure 29: Radial distributions of efficiency and entropy delta at different OPs and rotors.

Figure 30 shows iso-surfaces of the axial velocity to indicate areas of flow separation and blockage. At the last stable operating point of R0 ($\dot{m} = 28\ kg/s$, OP_{NS90}), high areas of blockage near the casing can be observed. For R1 and R5 these blockage areas are less

distinguished. At OP_{S90} low velocities along the whole span are visible, which is a result of the increasing shock intensity. This low energetic flow travels in the radial direction and accumulates in the trailing edge region of the tip, where it leads to a flow separation. For the optimized rotors this can be regarded as an additional effect influencing the stability.

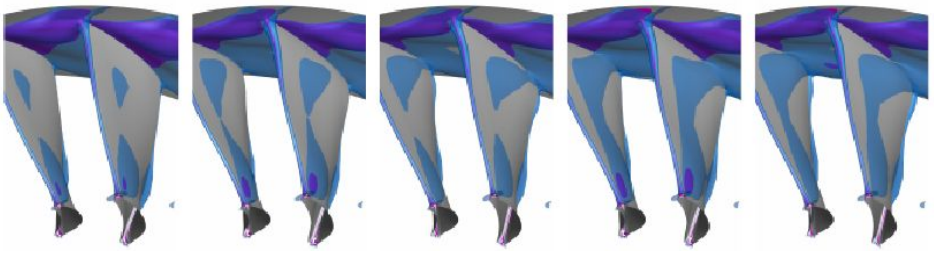

(a) R0 $\dot{m} = 28\ kg/s$ (b) R1 $\dot{m} = 28\ kg/s$ (c) R5 $\dot{m} = 28\ kg/s$ (d) R1 OP_{S90} (e) R5 OP_{S90}

Figure 30: Iso-surfaces of axial-velocity of 50m/s(light blue) and 0m/s (dark blue) for R0,R1 and R5 at OP_{NS90} and OP_{S90} (RANS simulations).

R1 and R5 represent the two extremes regarding the objectives, maximum efficiency (R5) and stability (R1). Combined with AxCT1 they nearly reach an equal stability margin.

Figure 31 shows similar iso-surface plots of axial velocity at OP_{S90} for both rotors with and without AxCT1. Without CT, R1 shows large areas of low energetic flow across the whole blade as compared to R5 without CT. This can be attributed to the fact that R1 has been optimized for stability and fails at a state where all blade sections are close to their limits. With CT, the areas of low energetic flow can be observed equally for R1 and R5, indicating an influence on the stability limit, as also observed without CTs.

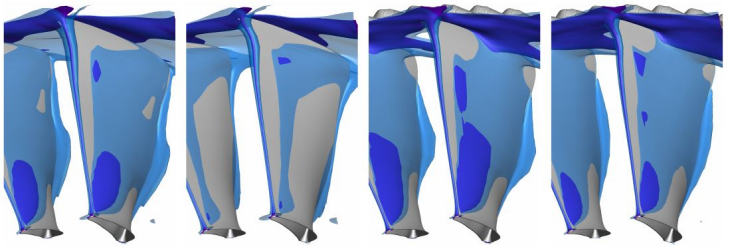

(a) R1 (b) R5 (c) R1+AxCT1 (d) R5+AxCT1

Figure 31: Iso-surfaces of axial-velocity of 50m/s(light blue) and 0m/s (dark blue) for R1 and R5 without and with AxCT1 at OP_{S90} (time averaged URANS simulations).

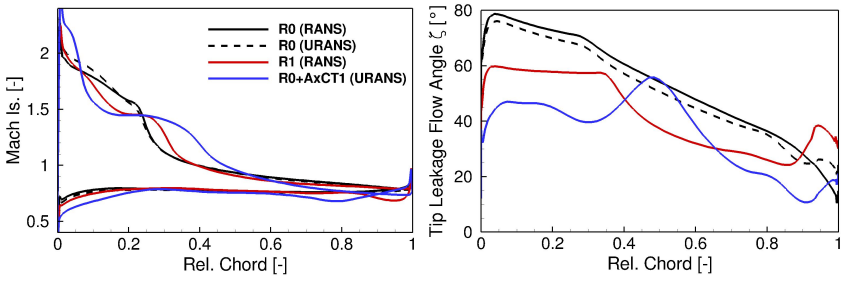

Figure 32: Isentropic Mach number and tip leakage flow angle distributions at OP_{NS90} (URANS, time average). Mach numbers at 90% span. ζ at mid-clearance.

It follows that with increasing stability margin, effects originating in lower blade areas develop an increasing influence that at some point can not be suppressed by axial-slots anymore. This explains the rather limited benefit of applying CTs to the reference configuration as compared to a rotor optimization improving the stability margin.

7.0 CONCLUSION

A method has been shown to perform efficient optimizations of rotors and CTs with a high accuracy in stability margin determination. The results of two optimizations, a rotor and a CT optimization, have been compared and Pareto-optimal designs of both optimizations have been combined to evaluate the overall potential of CTs for improved designs.

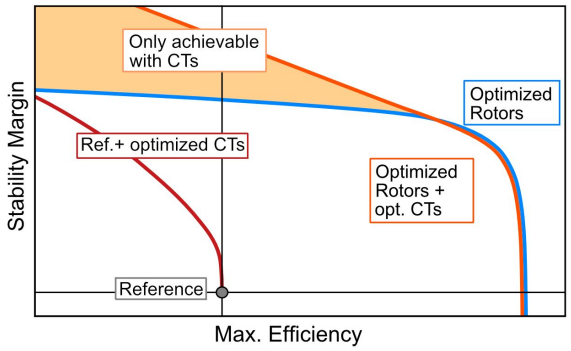

Figure 33: Schematic plot of improvements possible through different measures.

Figure 33 shows a sketch of the general results of this study. There exists an area in the stability margin and efficiency domain that can only be reached by designs with CTs. This area represents high values of stability margin. No designs with CTs can be achieved that dominate designs without CTs in terms of stability margin and efficiency at the same time.

Both approaches of increasing the stability margin, CT optimization and rotor optimization as well, show a similar influence on the tip flow regarding the tip leakage flow, throttling and hence, shock-vortex-interaction. Within a certain range of improvement an optimization of the rotor without an application of CTs is therefore capable of achieving satisfactory results regarding stability margin and efficiency.

The axial-slots, however, can further increase the stability margin to values that can not be obtained without CTs. This can be attributed to the known working principle of axial-slots, a removal of blockage fluid, its recirculation and injection into the main flow in the area of the developing tip-leakage-vortex. The influence on the time averaged tip-leakage flow is in some regards similar to what has been achieved by the rotor optimization, but of stronger intensity.

When reaching the stability limit, all designs with increased stability margin, regardless of with or without CT, show large areas of low momentum fluid behind the shock across the whole span. This flow travels in the radial direction towards the tip and accumulates in the downstream part of the blade influencing the tip leakage flow. It can be assumed that this flow has a significant influence on the stability and limits the capability of CTs to increase the stability margin. In future studies the blade design should therefore be optimized together with the CT design.

The effect of a CT-application on efficiency has been observed to be negative for all rotor designs of high efficiency. For a rotor design with low efficiency the application of CTs had no negative influence on efficiency. It is assumed that an efficiency-neutral design can only be achieved if the reference design without CTs shows considerable losses at tip that provide a potential to compensate the additional CT losses. This could especially be the case for small core stages with a high relative tip clearance. If the potential to compensate the CT-losses is not given, an application of CTs with the goal of an increased efficiency of the stage or compressor could only be achieved indirectly, by trading the gain in stability margin with an increased loading, e.g. through a reduction of blades.

REFERENCES

1. Hathaway MD. Passive Endwall Treatments for Enhancing Stability [Internet]. NASA; 2007 Jul. Report No.: TM-2007-214409, ARL-TR-3878, E-15688. Available: https://ntrs.nasa.gov/search.jsp?R=20070025023
2. Brignole GA, Danner FCT, Kau H-P. Time Resolved Simulation and Experimental Validation of the Flow in Axial Slot Casing Treatments for Transonic Axial Compressors. ASME Conference Proceedings. ASME; 2008. pp. 363–374. doi:10.1115/GT2008-50593
3. Johann E, Streit A, Brandstetter C. Auslegung einer Verdichterbeschaufelung zur Untersuchung von Instabilitäten und Abreißmechanismen an der Laufschaufelspitze - Verbundvorhaben COORETEC Turbo III Teilvorhaben 1.2.3A [Internet]. 2013. doi:10.2314/GBV:819852678
4. Inzenhofer A. Erhöhung der Leistungsdichte in mehrstufigen Verdichtern durch Impulsausblasung und Einsaugen: Schlussbericht: Teilverbundprojekt: 1. Verdichtung : Vorhaben Gruppe: 1.1 Effizienzsteigerung : Vorhaben: COOREFLEX 1.1.6b [Internet]. Technische Universität München; 2018. doi:10.2314/GBV:1047035537
5. Inzenhofer A, Guinet C, Hupfer A, Becker B, Grothe P, Heinichen F. Difference in the Working Principle of Axial Slot and Tip Blowing Casing Treatments. ASME Turbo Expo 2016: Turbomachinery Technical Conference and Exposition. Seoul, South Korea; 2016. doi:10.1115/GT2016-56966
6. Streit JA, Heinichen F, Kau H-P. Axial-Slot Casing Treatments Improve the Efficiency of Axial Flow Compressors: Aerodynamic Effects of a Rotor Redesign. ASME Turbo Expo 2013: Turbine Technical Conference and Exposition GT2013. American Society of Mechanical Engineers; 2013. doi:10.1115/GT2013-94975
7. Streit JA, Guinet C, Heinichen F, Kau HP. Trading excessive stall margin for efficiency: An alternative approach to axial-slot casing treatments for transonic compressors. ISUAAAT, Tokyo, Japan, Sept. 2012; 11–14.
8. Goinis G, Voß C, Aulich M. Automated Optimization of an Axial-Slot Type Casing Treatment for a Transonic Compressor. ASME Turbo Expo 2013: Turbine Technical Conference and Exposition. American Society of Mechanical Engineers; 2013. doi:10.1115/GT2013-94765
9. Goinis G, Nicke E. Optimizing Surge Margin and Efficiency of a Transonic Compressor. ASME Turbo Expo 2016: Turbomachinery Technical Conference and Exposition. American Society of Mechanical Engineers; 2016. doi:10.1115/GT2016-57896
10. Goinis G, Voß C, Aulich M. Circumferential grooves for a modern transonic compressor: aerodynamic effects, benefits and limitations. Proceedings of ETC, Lappeenranta, Finland. 2013;60. https://www.euroturbo.eu/paper/ETC2013-060.pdf
11. Inoue M, Kuroumaru M, Yoshida S, Minami T, Yamada K, Furukawa M. Effect of Tip Clearance on Stall Evolution Process in a Low-Speed Axial Compressor Stage. Volume 5: Turbo Expo 2004, Parts A and B. ASME; 2004. pp. 385–394. doi:10.1115/GT2004-53354
12. Yamada K, Kikuta H, Furukawa M, Gunjishima S, Hara Y. Effects of Tip Clearance on the Stall Inception Process in an Axial Compressor Rotor. Volume 6C: Turbomachinery. ASME; 2013. doi:10.1115/GT2013-95479
13. Yamada K, Furukawa M, Tamura Y, Saito S, Matsuoka A, Nakayama K. Large-Scale DES Analysis of Stall Inception Process in a Multi-Stage Axial Flow

Compressor. ASME Turbo Expo 2016: Turbomachinery Technical Conference and Exposition. American Society of Mechanical Engineers; 2016. doi:10.1115/GT2016-57104

14. Weichert SA, Day IJ. Detailed Measurements of Spike Formation in an Axial Compressor. J Turbomach. 2014;136. doi:10.1115/1.4025166

15. Pullan G, Young AM, Day IJ, Greitzer EM, Spakovszky ZS. Origins and Structure of Spike-Type Rotating Stall. J Turbomach. 2015;137: 051007. doi:10.1115/1.4028494

16. Lejon M, Andersson N, Sciences M, Ellbrant L. The surge margin of an axial compressor: estimations from steady state simulations. ISABE. 2017. pp. 1–13.

17. Goinis G, Voß C. Optimierung von transsonischen Verdichterstufen mit Gehäuseeinbauten : Abschlussbericht COORETEC-TURBO Forschungsvorhaben: Verbundprojekt: CO2-Reduktions-Technologien, Vorhaben-Nr. 1.1.5 [Internet]. Dt. Zentrum für Luft- und Raumfahrt, Inst. für Antriebstechnik; 2013. doi:10.2314/GBV:791239918

18. Ashcroft G, Heitkamp K, Kuegeler E. High-order accurate implicit runge-kutta schemes for the simulation of unsteady flow phenomena in turbomachinery. 5th European Conference on Computational Fluid Dynamics ECCOMAS CFD. Lisbon, Portugal; 2010.

19. Becker K, Heitkamp K, Kuegeler E. Recent progress in a hybrid-grid CFD solver for turbomachinery flows. 5th European Conference on Computational Fluid Dynamics ECCOMAS CFD. Lisbon, Portugal; 2010.

20. Voss C, Nicke E. Automatische Optimierung von Verdichterstufen : Fachlicher Abschlussbericht ; Verbundprojekt: CO2-Reduktion durch Effizienz ; Vorhabengruppe 1.1: Hocheffiziente Kompressoren für das CO2-freie Kraftwerk [Internet]. DLR; 2008. doi:10.2314/GBV:595025846

21. Aulich M, Voss C, Raitor T. Optimization strategies demonstrated on a transonic centrifugal compressor. ISROMAC. 2014. pp. 24–28.

22. Aulich M, Siller U. High-Dimensional Constrained Multiobjective Optimization of a Fan Stage. ASME 2011 Turbo Expo: Turbine Technical Conference and Exposition. American Society of Mechanical Engineers; 2011. pp. 1185–1196. doi:10.1115/GT2011-45618

23. Voß C, Aulich M, Raitor T. Metamodel assisted aeromechanical optimization of a transonic centrifugal compressor. 15th International Symposium on Transport Phenomena and Dynamics of Rotating Machinery, ISROMAC-15. 2014.

24. Reid L, Moore RD. Performance of Single-Stage Axial-Flow Transonic Compressor With Rotor and Stator Aspect Ratios of 1.19 and 1.26, Respectively, and With Design Pressure Ratio of 1.82. NASA, Lewis Research Center, Cleveland, Ohio; 1978.

25. Goinis G, Stollenwerk S, Nicke E, Kügeler E. Steady state versus time-accurate CFD in an automated airfoil section optimization of a counter rotating fan stage. Proceedings of the ASME Turbo Expo. 2011. doi:10.1115/GT2011-46190